THE UNIVERSITY of EDINBURGH

Edinburgh Research Explorer

Anisotropic dynamics and kinetic arrest of dense colloidal ellipsoids in the presence of an external field studied by differential dynamic microscopy

OPEN ACCESS

MATERIALS SCIENCE

Anisotropic dynamics and kinetic arrest of dense colloidal ellipsoids in the presence of an external field studied by differential dynamic microscopy

Antara Pal[1]*, Vincent A. Martinez[2], Thiago H. Ito[1], Jochen Arlt[2], Jérôme J. Crassous[1†], Wilson C. K. Poon[2], Peter Schurtenberger[1,3]*

Anisotropic dynamics on the colloidal length scale is ubiquitous in nature. Of particular interest is the dynamics of systems approaching a kinetically arrested state. The failure of classical techniques for investigating the dynamics of highly turbid suspensions has contributed toward the limited experimental information available up until now. Exploiting the recent developments in the technique of differential dynamic microscopy (DDM), we report the first experimental study of the anisotropic collective dynamics of colloidal ellipsoids with a magnetic hematite core over a wide concentration range approaching kinetic arrest. In addition, we have investigated the effect of an external magnetic field on the resulting anisotropic collective diffusion. We combine DDM with small-angle x-ray scattering and rheological measurements to locate the glass transition and to relate the collective short- and long-time diffusion coefficients to the structural correlations and the evolution of the zero shear viscosity as the system approaches an arrested state.

INTRODUCTION

Unlike their spherical counterparts, anisotropic particles exhibit a richer phase behavior with enhanced complexity due to their orientational degrees of freedom. In addition to the usual gas, liquid, crystal, and glass phases, anisotropic particles such as rods are known to exhibit liquid crystalline phases. While most of the existing studies address structural properties, less is known about the dynamic behavior of anisotropic particles. The most well-studied systems in this regard are perhaps colloidal rods and ellipsoids (1–9). However, because most of these studies involved particle tracking, they are therefore limited to quasi-2D (two dimension) and to self-diffusion. In bulk, several studies combining polarized and depolarized light scattering report the average translational and rotational diffusion coefficients (10–15) of different anisotropic particles. In these systems, multiple scattering and absorption of light at high concentrations make the measurement not only challenging but also sometimes impossible. As a result, most of the studies were carried out in the dilute regime, and a systematic description of the anisotropic dynamics approaching the ordered or arrested glassy phase is still lacking for bulk systems.

Theoretical studies on ellipsoidal particles predict a kinetic phase diagram as a function of packing fraction ϕ and aspect ratio ρ (16, 17). Depending on the aspect ratio, three types of glass transitions have been predicted, with the first one being the conventional cage driven one that is also found for spherical particles, while the other two have their origins related to the orientational degrees of freedom. For nonspherical particles, a glass phase is predicted consisting of nematic domains, where the interdomain orientations build an orientational glass. Experimentally, such an orientational glass has only been reported for a system of very long and thin rods (fd viruses) by Kang and Dhont (18) and Kang (19). Contrary to the prediction by Schilling et al. (16, 17), particle arrest and the freezing of the nematic domain texture were found to occur at the same concentration. The experiments thus reveal that for these long rods, there is a single glass transition, and both particle dynamics and the nematic domain texture dynamics arrest simultaneously. It is also important to point out that while the particles used by Kang et al. resemble rods rather than ellipsoids, at these large axial ratios, we would not expect notable differences in their behavior. The third type of glass transition is predicted for nearly spherical ellipsoids where the orientational degrees of freedom with odd parity flip and freeze independently from the positions. Recent simulations explored the dynamics around the glass transitions in 3D using ellipsoids of smaller aspect ratios (ρ = 1.25 prolate and 0.8 oblate). Consequently, the two-step glass transition with the orientational glass was not observed (20).

Despite a number of theoretical and simulation studies, opacity or turbidity apparently acts as a road block in the direct experimental investigations of concentrated anisotropic particles in 3D. This obstacle can sometimes be overcome by changing the solvent and matching the index of refraction of the particles, and in turn, it affects the interparticle interactions, which is not desirable. Differential dynamic microscopy (DDM) is a recently developed high-throughput technique that can overcome this limitation (21). In DDM, a time series of digital video images is acquired in bright-field or phase-contrast mode using a fast camera fitted to an ordinary optical microscope. The averaged power spectrum of the difference images is used to calculate the intermediate scattering function (ISF), which describes the dynamics of the system. DDM thus accesses the same dynamical quantity as dynamic light scattering (DLS), but in contrast to DLS, can also be applied to absorbing samples and is less affected by multiple scattering.

DDM has already been successfully used (22) to characterize the anisotropic dynamics of dilute colloidal ellipsoids over a wide range

[1]Division of Physical Chemistry, Department of Chemistry, Lund University, Lund, Sweden. [2]SUPA, School of Physics and Astronomy, The University of Edinburgh, Edinburgh, UK. [3]Lund Institute of Advanced Neutron and X-ray Science (LINXS), Lund University, Lund, Sweden.
*Corresponding author. Email: antara.pal@fkem1.lu.se (A.P.); peter.schurtenberger@fkem1.lu.se (P.S.)
†Present address: Institute of Physical Chemistry, RWTH Aachen University, Landoltweg 2, 52074 Aachen, Germany.

of scattering vectors **q**. We have exploited the advantage of DDM of not being limited by the opacity of the samples to explore the anisotropic dynamics of a bulk colloidal system in the collective regime. In this article, we report a detailed experimental study of the evolution of collective anisotropic dynamics of ellipsoidal colloids of aspect ratio $\rho = 3.76$ as a function of volume fraction. Through a combination of DDM and shear rheometry, we demonstrate the existence of a glass transition at a volume fraction of $\phi \approx 0.52$. DDM reveals several regimes for the collective dynamics in our ellipsoidal model system. At low concentrations, density fluctuations relax via a single decay process, which can be characterized by a collective diffusion coefficient D_s^c. However, above a critical concentration, due to interaction effects, a second decay process starts to develop, which can be quantified by a long-time collective diffusion coefficient D_l^c. We find that D_s^c can be scaled as $1/S(q_{\mathrm{DDM}})$, $S(q_{\mathrm{DDM}})$ being the structure factor measured at a q value, q_{DDM}, which lies in the same q range in which the DDM measurement has been done. Furthermore, D_l^c can be scaled as $1/\eta_0$, η_0 being the zero shear viscosity of the system as expected (23–25). Our experiments thus demonstrate that for hard ellipsoids in 3D, kinetic arrest occurs via a scenario that is analogous to the one encountered for hard spheres.

Being made up of hematite cores coated with silica shells, these particles are responsive toward an external magnetic field, which helps them to align along a particular direction. We can thus use a magnetic field to investigate the effects of a reduction in the rotational degrees of freedom on collective diffusion and the location of the glass transition. Although both D_s^c and D_l^c are isotropic at low magnetic fields at all concentrations, they start to develop anisotropic features as the field increases. This can be understood by the alignment of the particles in the presence of a magnetic field. This anisotropy in diffusion coefficients along different directions not only becomes maximum along and perpendicular to the field direction but also increases with the magnetic field. We show that not only the magnetic field results in an increasing decoupling of the particle diffusion parallel and perpendicular to the field direction but also additional small-angle x-ray scattering (SAXS) experiments reveal a possible change in the dominating mechanism that leads to dynamical arrest.

Theoretical background: Anisotropic diffusion of oriented prolate particles

For a dilute dispersion of noninteracting prolate ellipsoids with semi-long and short axes, a and b, the isotropic translational diffusion coefficient, D_{iso}, can be expressed as the average over the diffusion coefficients along the different axes (26)

$$D_{\mathrm{iso}} = \frac{1}{3}D_a + \frac{2}{3}D_b \tag{1}$$

where D_a and D_b are the translation diffusion coefficients along the long and short axis, respectively.

In the presence of an external magnetic field **B**, the individual silica-coated hematite (SCH) particles align with their magnetic moments **μ** being parallel to **B**. Because for hematite particles **μ** is perpendicular to the long axis of the ellipsoid, the particle orientation **a** is restricted to the plane perpendicular to **B** (27). However, **a** can still rotate around the direction of **B** (Fig. 1A) (27–29). As a result, the diffusion of the particles becomes anisotropic in nature (22). For noninteracting particles, one would expect that with increasing field, an alignment of the individual particles along with a slowing down of the dynamics measured parallel to **B** develops. The diffusion coefficient decreases from D_{iso} at zero field to a lower value D_b in the limit of high field when the particles are fully aligned. In contrast, the dynamics perpendicular to **B** is expected to increase from D_{iso} at zero field to $(D_a + D_b)/2$ at high field. The field-dependent diffusion coefficients, measured parallel and perpendicular to **B**, are given by (30)

$$D_{\parallel}(B) = D_{\mathrm{iso}} + \frac{2}{3}(D_a - D_b)S_2(h) \xrightarrow{B \to \infty} D_b$$
$$D_{\perp}(B) = D_{\mathrm{iso}} - \frac{1}{3}(D_a - D_b)S_2(h) \xrightarrow{B \to \infty} \frac{1}{2}(D_a + D_b) \tag{2}$$

with $S_2(h)$ being the second-order orientational order parameter and can be expressed as $S_2(h) = \left[\frac{3(\coth(h) - h^{-1})}{h} - 1\right]/2$, where h denotes the energy of the dipole moment μ normalized by $k_B T$ such as $h = \mu B/k_B T$. For a full description of the anisotropic diffusion, one needs to define an azimuthal diffusion coefficient $D(B, \theta)$ in terms of azimuthal angle θ with respect to the field direction such that it satisfies $D(B, \theta) = D_{\parallel}(B)$ for $\theta = 0$ and $D(B, \theta) = D_{\perp}(B)$ for $\theta = \pi/2$, which can be expressed as

$$D(B, \theta) = D_{\parallel}(B)\cos^2\theta + D_{\perp}(B)\sin^2\theta \tag{3}$$

This expression describes the anisotropic diffusion at any azimuthal angle θ with respect to the applied field.
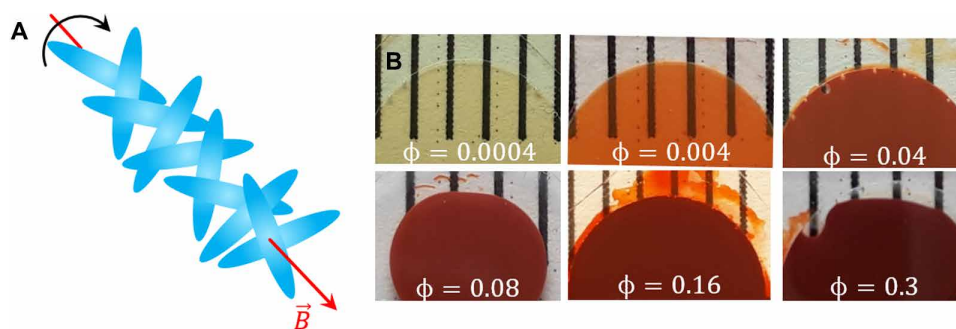
Fig. 1. Field-induced alignment and visual appearance of magnetic ellipsoidal particles. (**A**) Schematic of arrangement of ellipsoids in the presence of an external magnetic field with their shorter axes being parallel to the field direction. (**B**) Assortment of varied packing fractions of SCH suspension, which are confined between two glass coverslips separated by a spacer of width 120 μm. The opacity of the samples increases as the volume fraction ϕ increases, as illustrated with the black lines on a paper background positioned behind the samples, which become invisible for volume fractions above ϕ = 0.004 (photo credit: Antara Pal, Lund University).

RESULTS AND DISCUSSION

In DDM, the intensity fluctuations are analyzed from the spatial Fourier transform of a sequence of images to obtain the power spectrum, $g(\mathbf{q}, \tau)$. $g(\mathbf{q}, \tau)$ is directly related to the ISF, $f(\mathbf{q}, \tau)$, where $\mathbf{q}$ is the wave vector of the fluctuations being probed and τ is the delay time (21, 31–33). The ISF, which represents the density-density time correlation function, is a measure of the dynamics on the spatial scale $2\pi/q$. By analyzing the ISF in different azimuthal directions with respect to the applied field $\mathbf{B}$, we can determine the effective translational diffusion coefficients, $D(B, \theta)$, of the particles as a function of $\mathbf{B}$. In the version of DDM we implement (22, 32, 33), the incident light is completely incoherent, and the Fourier transform of the intensity correlation function of the images is directly related to the ISF by

$$g(q, \theta, \tau) = A(q, \theta)\left[1 - f(q, \theta, \tau)\right] + \widetilde{B}(q, \theta) \tag{4}$$

where $A(q, \theta)$ is related to the transfer function of the optical image system and the sample structure imaged and $\widetilde{B}(q, \theta)$ is related to the camera noise. In another version of DDM (21, 31), semicoherent incident light from a small aperture was used so that the detailed physics is somewhat different.

In the current study, we have explored the dynamics of SCH particles over a wide range of volume fraction, ϕ, starting from $\phi = 0.0002$ to $\phi = 0.51$ (details of particles synthesis and characterization as well as the volume fraction calculation are provided in Materials and Methods). Figure 1B illustrates the increased turbidity of the dispersion with ϕ, leading to almost opaque samples above

$\phi = 0.04$. As a result, none of the traditional techniques could be used to study their dynamics but DDM. Depending on the nature of $g(q, \tau)$, the whole concentration range can be divided into three regimes: dilute, semi-dilute, and concentrated.

Dilute regime: $0.002 \leq \phi < 0.04$

A dilute SCH dispersion ($\phi = 0.0002$) was first examined following the methodology described by Reufer *et al.* (22). At these concentrations, the particles are freely diffusive in nature, and the corresponding ISF along a particular direction can be described by a single exponential relaxation mode as

$$f(q, \tau) = \exp\left(-\tau/\tau_1\right) \tag{5}$$

where τ_1 is the relaxation time, which is related to the diffusion coefficient D as $D = 1/q^2\tau_1$. The diffusion coefficients of the particles in the different azimuthal directions at a field value B, $D(B, \theta)$, were then obtained by fitting the experimentally obtained $g(q, \tau)$ in different directions with Eqs. 4 and 5. Figure 2A shows a representative set of experimental $g(q, \tau)$'s at different q's at an azimuthal angle $\theta = -10°$ along with the fits, covering the range $2\ \mu m^{-1} < q < 5\ \mu m^{-1}$. The diffusion coefficient is independent of q in the aforementioned q range, as one can see in fig. S1. At zero magnetic field, the particles were found to be isotropically diffusive, as $D(B, \theta)$ was found to be constant over all the azimuthal angles with $D(B = 0, \theta) = D_{iso} = 2.15\ \mu m^2/s$ (Fig. 2B, first blue curve). This value is in good agreement with the diffusion coefficient determined by DLS as $D_{iso} = 2.24\ \mu m^2/s$.
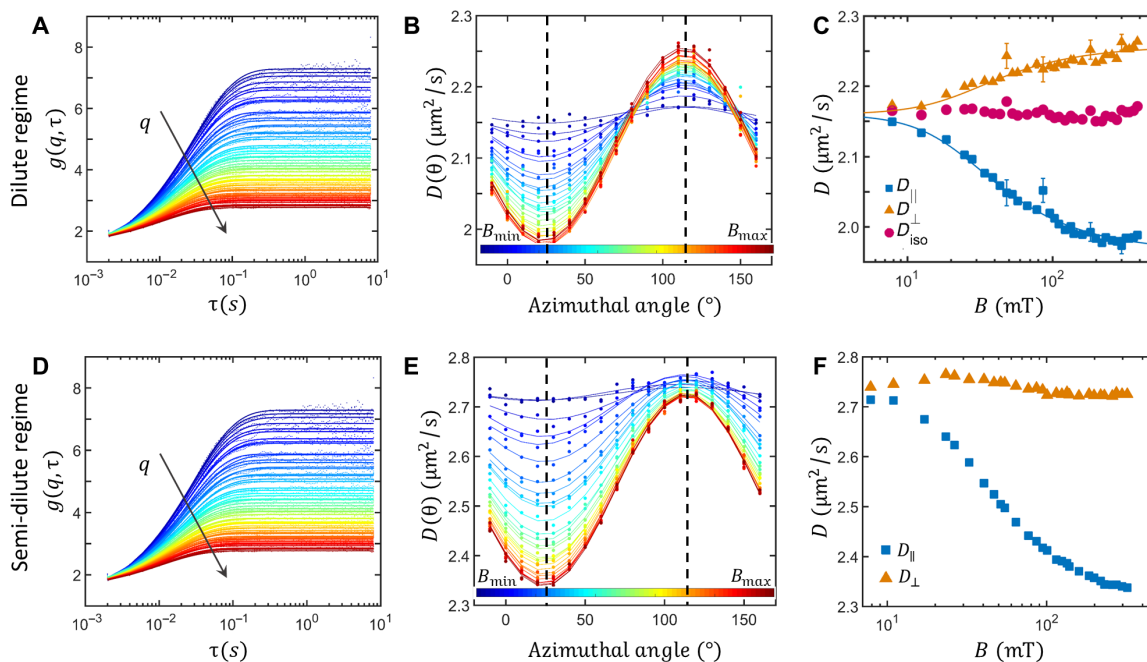

Fig. 2. Anisotropic dynamics in the dilute and semi-dilute regime. (Top) Dilute sample of volume fraction $\phi = 0.002$: (**A**) Variation of $g(q, \tau)$ as a function of delay time, τ, at different wave vectors q ($2\ \mu m^{-1} < q < 5\ \mu m^{-1}$) at an azimuthal angle $\theta = -10°$. Symbols show the experimental data, while the lines represent the fits with Eq. 5. q increases from blue to red. (**B**) Variation of diffusion coefficients, $D(B, \theta)$, as a function of azimuthal angle θ at different magnetic fields, which increases from blue (7.9 mT) to red (340 mT). The external magnetic field was applied at an angle $\theta \sim 25°$. (**C**) Variation of diffusion coefficients along, $D_{\parallel}$, and perpendicular, $D_{\perp}$, to the applied magnetic field (symbols) along with the fitting with Eq. 2 (solid line). D_{iso} is also shown. (Bottom) Semi-dilute sample of volume fraction $\phi = 0.041$: (**D**) Variation of $g(q, \tau)$ as a function of delay time, τ, at different wave vectors q ($2\ \mu m^{-1} < q < 5\ \mu m^{-1}$). Symbols show the experimental data, while the lines represent the fit with Eq. 6. q increases from blue to red. (**E**) Variation of diffusion coefficients, $D(\theta)$, as a function of azimuthal angle θ at different magnetic fields, which increases from blue to red. (**F**) Variation of diffusion coefficients along, $D_{\parallel}$, and perpendicular, $D_{\perp}$, to the applied magnetic field.

Upon increasing the amplitude of the magnetic field, the alignment of the particles perpendicular to the field is promoted, which is manifested by the stronger decoupling of the diffusion coefficient along and perpendicular to the field (Fig. 2C). The particles were found to start to align at about 15 mT and were almost fully aligned for $B > 300$ mT. A sinusoidal shape was observed for $D(B, \theta)$ as a function of θ that can be well described by Eq. 3 (Fig. 2B), which allows us to obtain the values of $D_\parallel$ and $D_\perp$ as a function of B. According to the theoretical predictions, $D_\perp(B)$ increases and $D_\parallel(B)$ decreases with field satisfying Eq. 2, which can be observed in Fig. 2C.

In addition, the measurements with decreasing fields superimposed within experimental error with those obtained for increasing fields, confirming that the particles get reversibly aligned at these concentrations (fig. S2). By fitting Eq. 2 to the observed $D_\parallel$ and $D_\perp$ (Fig. 2C), D_a and D_b were determined to be $D_a = 2.94$ $\mu m^2/s$ and $D_b = 1.77$ $\mu m^2/s$. The expected value for D_a and D_b based on the size of the particles are 2.95 and 2.32 $\mu m^2/s$, respectively. The origin of the discrepancy between the observed and expected value for D_b is discussed by Reufer et al. (22). These authors have argued that for comparable systems, particle sizes obtained by transmission electron microscopy (TEM) often suffer from the chosen threshold to find the particle contours and that this introduces a systematic error in the calculation of the expected D values. Moreover, the calculations assume perfect prolate shape, and the small geometrical imperfections at the tips of the ellipsoids also contribute to this discrepancy between measured and calculated values. Similar results were found up to $\phi = 0.04$.

Semi-dilute regime: 0.04 < φ < 0.21
As the volume fraction reaches a value around $\phi = 0.04$, the particles start to noticeably interact with each other, which, in turn, affects their dynamics. The ISF along a particular direction, $f(q, \tau)$, can no longer be described by a single exponential but with a stretched exponential

$$f(q,\tau) = \exp\left\{-(\tau/\tau_1)^{\beta_1}\right\} \qquad (6)$$

where β_1 is the stretching exponent. The fact that $\beta < 1$ indicates the presence of more than one relaxation process, and the resulting $D = 1/q^2\tau$ should then only be considered as an effective diffusion coefficient that represents the characteristic time scale of the system (variation of β as a function of ϕ is shown in fig. S3). Although we could not observe much difference in $g(q, \tau)$ (Fig. 2D) in comparison with the dilute regime, the effect is prominent in azimuthal diffusion coefficients $D(B, \theta)$ at high fields (Fig. 2, E and F). One can observe that with increasing field, $D_\parallel(B)$ still decreases as in the previous case. However, for $D_\perp(B)$, the observation is quite different. With increasing field, it first increases until around 30 mT and then starts to decrease slowly (Fig. 2F). The initial increase is due to the alignment of the short axis of the particles along the field. However, the field-induced alignment freezes one of the rotational degrees of freedom, which, in turn, affects the effective volume fraction of the system. Because the effective excluded volume of an aligned prolate is smaller than that of a randomly oriented one, the aligned system has a lower effective volume fraction than the actual one, which makes $D_\perp(B)$ decrease at higher fields (Fig. 2F).

Concentrated regime: 0.21 < φ < 0.51
In the concentrated regime, a second slow relaxation mode starts to develop in $g(q, \tau)$ (Fig. 3A). This new relaxation mode is associated with the structural rearrangements of the cages formed due to the crowding of the particles, while the fast mode represents the rattling inside the cages (17). At this concentration range, $f(q, \tau)$ can be well expressed by a double stretched exponential function representing two different relaxation modes with two different characteristic time scales, τ_1 and τ_2, as

$$f(q,\tau) = \alpha \exp\left\{-(\tau/\tau_1)^{\beta_1}\right\} + (1-\alpha)\exp\left\{-(\tau/\tau_2)^{\beta_2}\right\} \qquad (7)$$
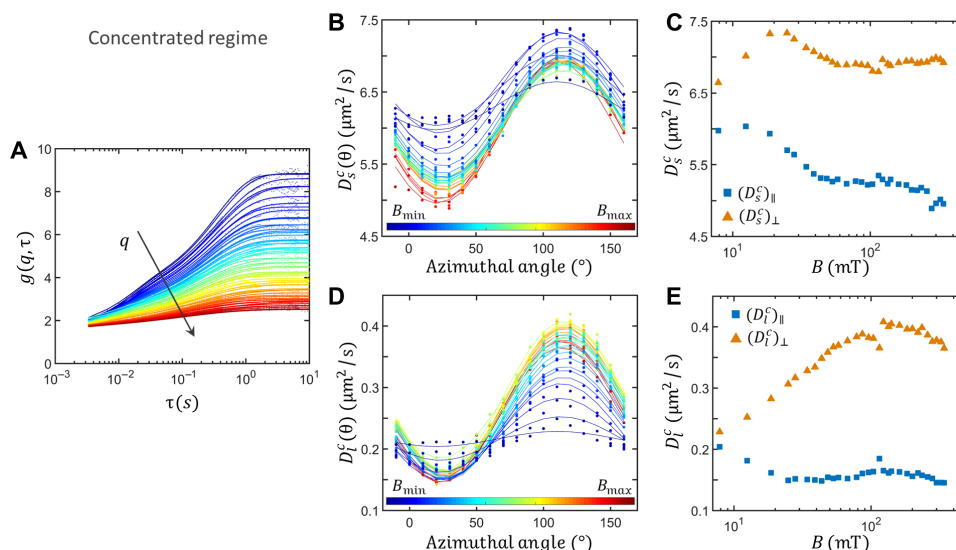

Fig. 3. Anisotropic dynamics in the concentrated regime. Concentrated sample of volume fraction $\phi = 0.48$: (**A**) Variation of $g(q, \tau)$ as a function of delay time, τ, at different wave vectors q (2 $\mu m^{-1} < q < 5$ μm^{-1}). Symbols show the experimental data, while the lines represent the fit with the equation (Eq. 7). q increases from blue to red. (**B**) Variation of short-time diffusion coefficients, $D_s^c(\theta)$, as a function of azimuthal angle θ at different magnetic fields, which increases from blue to red. (**C**) Variation of the short-time diffusion coefficients along and perpendicular to the applied magnetic field. (**D**) Variation of the long-time diffusion coefficients, $D_l^c(\theta)$, as a function of azimuthal angle θ at different magnetic fields. (**E**) Variation of long-time diffusion coefficients along and perpendicular to the applied magnetic field.

τ_1 and τ_2 can be related to two different diffusion coefficients, namely, the short-time diffusion coefficient, $D_s^c(B, \theta)$, and the long-time diffusion coefficient, $D_l^c(B, \theta)$.

With increasing field, $D_s^c(B, \theta)$ shows strong decoupling as a function of azimuthal angles θ, which can be well expressed by Eq. 3 (Fig. 3, B and C). For the slow relaxation mode related to the cage relaxation, the diffusion coefficient $D_l^c(B, \theta)$ also has an azimuthal decoupling as a function of θ (Fig. 3D). However, the variation of $D_{l\parallel}^c(B)$ and $D_{l\perp}^c(B)$ with increasing field is very different from that for the fast relaxation mode (Fig. 3E). In this case, $D_{l\parallel}^c(B)$ decreases with increasing field and finally gets saturated, while $D_{l\perp}^c(B)$ increases continuously up to a very high value and then starts to decrease. This is an indication that the cage dynamics is also anisotropic. Because the individual particle already tries to align perpendicular to the field, it is much easier to rearrange a cage along that direction than parallel to the field.

The average diffusion coefficients can be obtained by taking an azimuthal average of the diffusion coefficients. At the lowest field, the normalized average short-time diffusion coefficient, $(D_s^c)_{\text{avg}}/D_0$, strongly increases as the system approaches a kinetically arrested state as shown in Fig. 4A (red circles), where D_0 is the free particle diffusion coefficient. The variation of $(D_s^c)_{\text{avg}}/D_0$ with ϕ is expected to follow the well-known expression (25, 34)

$$\frac{(D_s^c)_{\text{avg}}}{D_0} = \frac{H(q)}{S(q)} \tag{8}$$

[$H(q)$ and $S(q)$ are the hydrodynamic function and static structure factor, respectively] as is evident from Fig. 4A, which also shows the variation of $1/S(q_{\text{DDM}})$ as a function of ϕ (black squares). $S(q_{\text{DDM}})$'s at $q_{\text{DDM}} = 10\ \mu m^{-1}$ (which is comparable to the wave numbers probed by DDM) for different concentrations have been experimentally measured by SAXS (fig. S4). Experimentally, similar behavior has also been reported for spherical colloidal systems as well as for globular proteins, polymers, and flexible rods (25, 35–39).

The normalized average long-time collective diffusion coefficient, $(D_l^c)_{\text{avg}}/D_0$, is significantly smaller than the short-time diffusion coefficient as expected. In contrast to $(D_s^c)_{\text{avg}}/D_0$, $(D_l^c)_{\text{avg}}/D_0$ decreases markedly as the system is approaching an arrested state (Fig. 4B, black squares). Because $(D_l^c)_{\text{avg}}/D_0$ is associated with structural rearrangement, it inversely scales with the reduced zero shear

viscosity of the system given by η_0/η_{sol}, where η_0 is the zero shear viscosity of the sample and η_{sol} is the viscosity of the solvent (Fig. 4B, magenta circles). The increase in viscosity of glass-forming molecular liquids with decreasing temperature is well described by the Vogel-Fulcher-Tammann (VFT) law (40–42). To use the VFT law for colloidal systems, temperature should be replaced by $1/\phi$, because the colloidal volume fraction ϕ plays a similar role as the temperature does for molecular glasses. The modified VFT expression $\eta_0 = \eta_{\text{sol}} \exp\left(\frac{F\phi}{\phi_{\text{max}} - \phi}\right)$ phenomenologically describes the rise in the viscosity of a colloidal suspension with ϕ and its marked increase at $\phi = \phi_{\text{max}}$ (43, 44). Here, $1/F$ is the fragility that accounts for the deviation of the viscosity from an Arrhenius dependence on ϕ as the sample approaches the arrested state. For our case, we find ϕ_{max} to be 0.52 (Fig. 4B, blue dashed line). Variation of viscosity as a function of ϕ in colloidal suspensions has also frequently been fitted with the Quemada relationship $\eta_0 = \eta_{\text{sol}}\left(1 - \frac{\phi}{\phi_{\text{max}}}\right)^{-\alpha}$ to predict the volume fraction ϕ_{max} at which η diverges (45) (α is the parameter characterizing the singular behavior and is ~2 for many colloidal systems). By considering the Quemada model, ϕ_{max} is also found to be 0.52 (Fig. 4B, orange dashed line). Similar concentration-dependent behavior for $(D_s^c)_{\text{avg}}$ and $(D_l^c)_{\text{avg}}$ has been reported for another anisotropic colloidal system, namely, charged gibbsite platelets (14). Our results thus indicate that collective dynamics of suspensions of hard ellipsoids show a behavior that is quite similar to that of hard sphere suspensions upon approaching a dynamic arrest, where caging is the dominant mechanism. Given the close proximity of the arrest transition with $\phi_{\text{max}} \approx 0.52$ to the predictions for the isotropic-nematic transition for ellipsoids with an axial ratio of $\rho = 3.76$ from simulations (46), such an arrest scenario is not obvious (17), and we will further discuss this below when describing the effect of an applied magnetic field.

In the presence of an external field, the decoupling of the diffusion coefficients between parallel and perpendicular directions increases with ϕ (Fig. 5). The decoupling behavior for the short-time dynamics can be quantified with the help of a decoupling parameter $(D_\perp - D_\parallel)/(D_s^c)_{\text{avg}}$. One can observe that for higher magnetic fields, the decoupling starts at very low concentrations, and it increases with increasing ϕ and finally reaches a maximum at the highest field for the highest concentration.
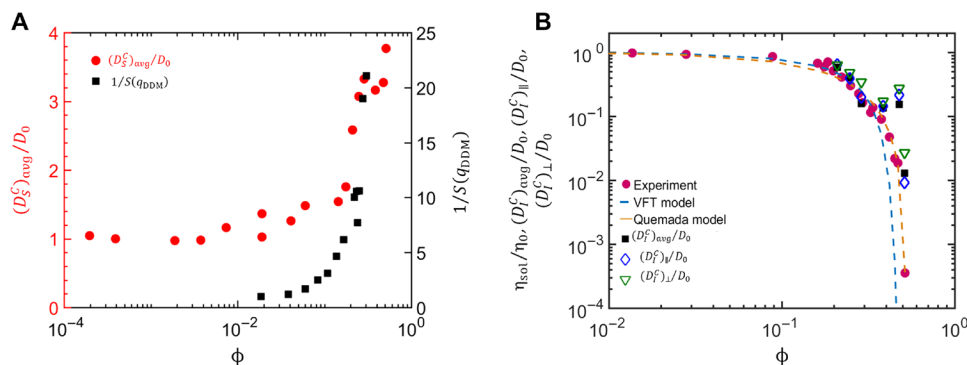

Fig. 4. Concentration dependence of dynamic and structural properties. (**A**) Variation of normalized average short time diffusion coefficient (red circles) and $1/S(q_{\text{DDM}})$ at $q_{\text{DDM}} = 10\ \mu m^{-1}$ (black squares) with ϕ at the lowest filed. (**B**) Variation of normalized average long-time diffusion coefficient with ϕ (black squares) at the lowest field; magenta circles show experimentally observed variation of inverse of normalized zero shear viscosity with ϕ, while the dashed orange and blue lines represent the fit with Quemada and VFT models, respectively. Variation of normalized long-time diffusion coefficients with ϕ, along parallel (blue diamond) and perpendicular (green triangle) to the field at high (340 mT) magnetic field.
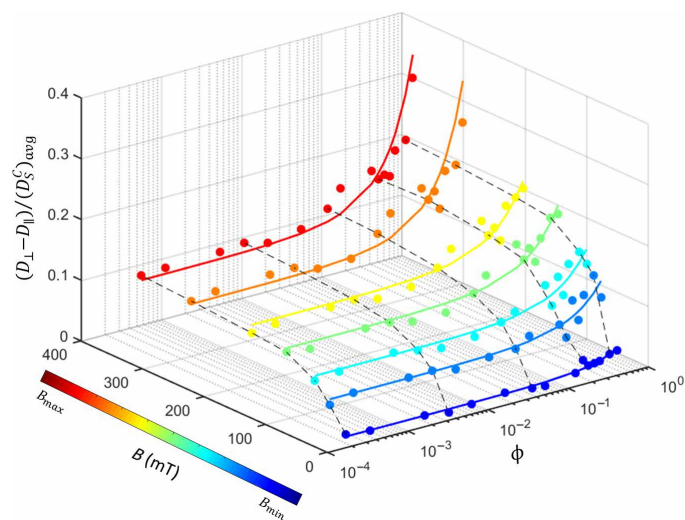
Fig. 5. Field-induced anisotropy of short-time diffusion and its concentration dependence. Observed variation of the decoupling parameter $(D_\perp - D_\parallel)/(D_S^c)_{avg}$ as a function of external field and ϕ (symbols). The lines are guide to the eyes and not a fit.

Fig. 6. Local structure based on small-angle scattering. 2D scattering pattern for $\phi = 0.3$ at (**A**) 7 mT and (**B**) 300 mT. Panels (**C**) and (**D**) represent two models that are based on the diffraction patterns to understand the local structures at low and high fields.

In the absence of a magnetic field, simulation (*17*) has predicted the formation of domains with local nematic order to explain the slowing down mechanism for aspect ratios $\rho > 2$. However, at low magnetic fields, the SAXS experiments provide no evidence for any nematic ordering as demonstrated with the 2D diffraction patterns shown in (Fig. 6A). This changes markedly when going to larger field strength, where a corresponding nematic order becomes apparent (Fig. 6B). The fact that we find no evidence for the formation of nematic domains in the absence of a field indicates that the slowing down of long-time diffusion and the occurrence of an arrest transition are the results of cage formation only. The question then remains whether this scenario changes in the presence of a high field, where the SAXS experiments reveal the formation of nematic domains. At this point, it is worth looking more into the volume fraction dependence of the anisotropic diffusion coefficients perpendicular and parallel to the field. Their normalized values $(D_l^c)_\perp/D_0$ and $(D_l^c)_\parallel/D_0$ are also shown in Fig. 4B and appear to follow the same scaling relation with volume fraction as previously observed for the average normalized long-time diffusion coefficient $(D_l^c)_{avg}/D_0$ in the absence of a field. Note that here we have normalized the anisotropic diffusion coefficients with an additional constant factor such that $(D_l^c)_\perp/D_0$ and $(D_l^c)_\parallel/D_0$ superimpose with $(D_l^c)_{avg}/D_0$ at the lowest concentration where long-time diffusion could be measured to focus on the effect of volume fraction near arrest only. The data shown in Fig. 4B indicate that dynamical arrest is governed by the formation of nearest-neighbor cages only in all cases, irrespective of whether nematic domains are present or not. These findings are in contrast to the previously described simulations (*17*), which predicted that for the axial ratio chosen in this study, arrest should be linked to the formation of nematic domains. While the actual cage relaxation dynamics may be influenced by the variation of the local order imposed by the applied magnetic field (Fig. 6, C and D), these variations are not visible within the statistical error of the data shown in Fig. 4B.
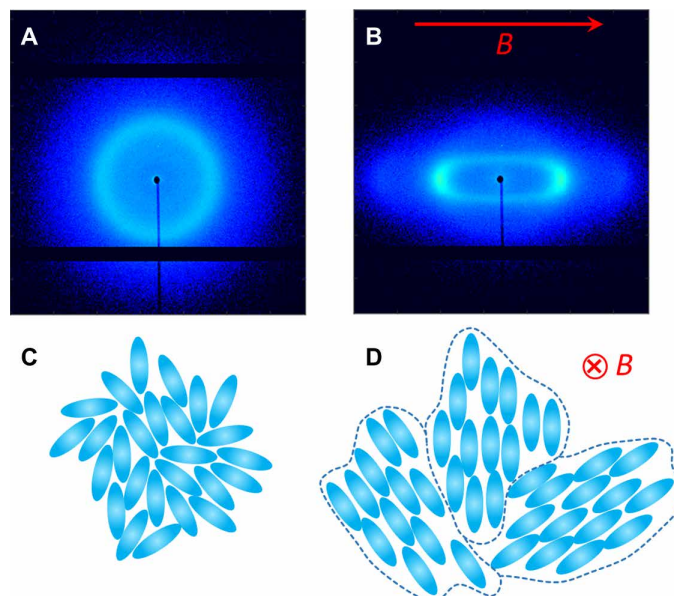
CONCLUSION

We have studied the field-induced anisotropic collective dynamics of colloidal ellipsoids over a broad concentration range by exploiting the recently developed technique DDM. The chosen model system, hematite-silica core-shell particles, has a number of advantages. It not only provides us with a simple synthesis route toward quite monodisperse prolate particles with tunable axial ratios but also allows us to modify the rotational degrees of freedom using external magnetic fields. However, the very high scattering cross section for visible light combined with a strong absorption has previously made it impossible to use the traditional optical tools such as DLS or confocal microscopy to study diffusion at high concentrations and thus characterize the arrest transition expected to occur at high packing fractions. Our work now demonstrates that DDM can be extended to study samples with anisotropic dynamics in the limit of high turbidity and high absorption.

Although the literature is replete with simulations concerning the glass transition for ellipsoidal particles, there has been an almost complete lack of experimental information on these systems. The only study we are aware of for the ellipsoidal glass transition in bulk is based on rheological measurements (*45*) for an axial ratio $\rho = 4.8$, and no information on collective dynamics and complementary structural information that would provide further insight into the underlying arrest scenario has so far been presented. It is for this reason that we have performed a systematic study of the structural and dynamic properties of a model ellipsoid system using a combination of DDM, SAXS, and rheology. This has allowed us to study collective diffusion in different concentration regimes and particularly look for the typical signatures of an arrest transition in the ISF measured by DDM. We have characterized both short- and long-time collective diffusion upon approaching kinetic arrest. In the absence of an applied magnetic field, we found that the inverse reduced zero shear viscosity and the long-time collective diffusion

coefficient are following the same characteristic scaling relation that has previously been used to reproduce these quantities in hard sphere systems. Moreover, we have been able to demonstrate that the arrest transition for these ellipsoids is not linked to the formation of nematic domains, quite in contrast to previous computer simulations of ellipsoids with comparable axial ratios (*17*). Furthermore, we have also shown that the arrest mechanism appears to be similar in the presence and absence of the external field and linked to caging and not influenced by the field-induced formation of nematic domains at volume fractions significantly smaller than $\phi_{max} \approx 0.52$.

The combination of DDM and SAXS in the presence of an external magnetic field has shown high potential for future studies. While more work will be required using additional complementary techniques, our results on the field dependence of the anisotropic short- and long-time collective diffusion and the average structure indicate no change in the dominating arrest mechanism with increasing field strength, despite the fact that nematic domains form at high field strengths already before arrest. Here, future experiments using x-ray photon correlation spectroscopy as a function of field strength would allow us to probe the anisotropic short- and long-time collective dynamics at much shorter characteristic length scales of order of the nearest-neighbor distance and using very small scattering volumes (*47*). This should then allow us to investigate the dynamics of cage relaxation in the vicinity of the arrest transition and its dependence on a field-induced local order and the formation of nematic domains. Moreover, a systematic investigation of the structural and dynamic properties of concentrated suspensions of prolate ellipsoids when approaching kinetic arrest and the underlying arrest mechanisms as a function of axial ratio is needed and will allow us to test the existing literature on simulations.

Until recently, such an endeavor would have been perceived as very difficult experimentally due to a lack of available model systems when using the traditional experimental tools such as DLS or confocal microscopy. However, our study has shown that the type of anisotropic systems that can be used to study the colloidal glass transition can now be greatly extended, as turbidity becomes a minor issue when using DDM. This opens new avenues for exploring the dynamics of strongly interacting colloidal systems with a large variety of shapes and chemical compositions. We believe that our results will inspire future experimental studies on concentrated anisotropic particles and provide the basis for comparison with theory and simulation.

MATERIALS AND METHODS
Synthesis of the SCH
Spindle Fe_2O_3 hematites were first synthesized in water following the approach described by Ocaña *et al.* (*48*) and further coated with a thin silica layer in ethanol using the method developed by Graf *et al.* (*49*). After purification by repeated centrifugation/redispersion cycles in water, the SCHs were kept in water as a stock dispersion of 2.5 weight %. Details of the synthesis and characterization of similar particles can be found elsewhere (*28, 29*).

Characterization of SCHs
The size and shape characterization of the ellipsoidal colloids were carried out using TEM (TEM-CM100 microscope from Philips operating at 100 keV). Particle size distributions were calculated by measuring at least 100 particles from TEM images using ImageJ. The average particle semi-long, *a*, and semi-short, *b*, axes are found to be $a = 148.5$ nm and $b = 39.5$ nm, leading to an aspect ratio of $\rho = 3.76$.

Sample preparation
The concentrated SCH dispersions were prepared by centrifuging the stock dispersion to the desired weight fraction, whereas more dilute dispersions were obtained by diluting more concentrated samples. To ensure the proper redispersion, the dense samples were sonicated for 24 hours in a thermostated sonication bath. DDM samples were prepared by placing a 9-μl drop of the sample between two coverslips separated by a 120-μm spacer. Each sample was sonicated for about 2 hours before the preparation of the DDM sample cell. To avoid an eventual drift of the denser and more viscous dispersions, cells filled with dense samples were let to relax typically for 12 to 24 hours in a water-saturated atmosphere.

To convert the weight fraction into volume fraction, the density of a single core-shell ellipsoidal particle was determined with two pair of semiaxes, *a* and *b*, representing the long and short axis, respectively. One pair is related with the core dimensions, a_{core} and b_{core}, while the other is related with the whole particle dimension, a_{part} and b_{part}. The core is composed of hematite with a density, ρ_{hem}, and the shell is composed of silica with a density, ρ_{sil}. Because both silica and hematite are porous materials, it is necessary to include a porosity contribution in terms of volume fraction with respect to the overall particle volume. The porosity in the core (ϕ_{pores}^{core}) and in the shell (ϕ_{pores}^{shell}) are 0.26 (*28*) and 0.32 (*50*), respectively. Despite of the fact that there are accessible and inaccessible pores (*50*), we assumed that all the pores in the core are filled with silica, while in the shell, they are filled with the solvent, which is water in our case with density ρ_{wtr}. Therefore, the overall density of the particle is given by

$$\rho_{part} = \frac{1}{a_{part}b_{part}^2}\Big[a_{core}b_{core}^2\Big\{\rho_{sil}\phi_{pores}^{core} + \rho_{hem}\Big(1 - \phi_{pores}^{core}\Big)\Big\} + \Big(a_{part}b_{part}^2 - a_{core}b_{core}^2\Big)\Big\{\rho_{wtr}\phi_{pores}^{shell} + \rho_{sil}\Big(1 - \phi_{pores}^{shell}\Big)\Big\}\Big]$$

(9)

Considering the densities, $\rho_{sil} = 2.06$ g cm^{-3}, $\rho_{hem} = 5.26$ g cm^{-3}, and $\rho_{wtr} = 1.00$ g cm^{-3} (*28*), and the dimensions from TEM as $a_{core} = 131$ nm, $b_{core} = 24.5$ nm, $a_{part} = 148.5$ nm, and $b_{part} = 39.5$ nm, a particle density (ρ_{part}) of 2.64 g cm^{-3} can be observed. The following expression can be used to calculate the volume fraction based on the densities of the particles and the solvent, and the weight fraction (χ_{part}) for each sample

$$\phi_{part} = \frac{\chi_{part}/\rho_{part}}{\big(\chi_{part}/\rho_{part}\big) + \Big[(1-\chi_{part})/\rho_{wtr}\Big] - \phi_{pores}^{shell}\big(\big(a_{part}b_{part}^2 - a_{core}b_{core}^2\big)/a_{part}b_{part}^2\big)\big(\chi_{part}/\rho_{part}\big)}$$

(10)

Experimental technique I: DDM
The DDM setup consists of an inverted optical microscope (Nikon Eclipse TE200) equipped with a fast camera (Mikrotron). The samples were imaged with a 40× objective in phase contrast mode. The sample stage was modified to install a solid core electromagnet connected to a dc power source (0 to 2.7 A). To prevent an excessive heating of the coils, the electromagnet was water-cooled using an external thermostat. The magnetic field was measured at the sample position using a tesla meter

(TL Atomic SMS 102), and the applied magnetic field in the sample was derived from the calibration of the measured magnetic field to the applied current. The measurements were performed with increasing and then decreasing magnetic fields from 7.9 to 380.0 mT, 7.9 mT being the remanent magnetic field for the electromagnet. The temperature of the sample was maintained with an accuracy of 0.1°C using a homemade sample holder connected to another thermostat. Depending on the concentration of the samples, the data acquisition mode has been varied from 200 to 500 frames/s.

Variation of diffusion coefficient as a function of q
In the range $2\,\mu m^{-1} < q < 5\,\mu m^{-1}$, the diffusion coefficient is independent of q. In fig. S1, we have plotted $f(q, \tau)$ as a function of $\tau . q^2$ for different q values, and the collapsing of all of them indicates the same fact.

Reversibility of diffusion coefficients
In the dilute regime, the diffusion coefficients measured during increasing the field almost superimposed with that measured while decreasing the field, which is shown in fig. S2.

Variation of stretching exponent β as a function of ϕ
In the semi-dilute and concentrated regimes, we have used single and double stretched exponential function(s) to describe the ISF. We find the stretching parameter β to be less than 1 (fig. S3). This indicates the presence of more than one single relaxation processes, although there is no visual appearance of that in $g(q, \tau)$ (Fig. 2D). The presence of more than one single relaxation processes becomes evident once the need to use double stretched exponential functions for concentrated regime arises. In this scenario, we observed the value of β_1 abruptly acquiring a higher value as can be observed in fig. S3.

Experimental technique II: SAXS
SAXS experiments were carried out at the cSAXS beamline of the Swiss Light Source (Paul Scherrer Institute, Switzerland) with a sample-detector distance of 7.160 m and an energy of 8.5 keV (corresponding to a wavelength of λ = 0.1459 nm). The scattering patterns were recorded on a single-photon counting PILATUS detector (1475 pixels × 1679 pixels). The samples with different concentrations were sealed in glass capillaries of 1 mm diameter and 0.1 mm wall thickness and investigated at room temperature. A horizontal magnetic field was produced with a water-thermostated electromagnet such that the field lines were always normal to the incident beam. The structure factor was calculated by dividing the scattered intensity I with the experimentally obtained form factor $F(q)$ (fig. S4). The variation of $1/S(q)$ for different concentrations (shown in Fig. 4A) has been calculated at $q_{DDM} = 10\,\mu m^{-1}$ (shown by dashed vertical line).

Experimental technique III: Rheology
The rheological measurement was done by an ARES-RFS (rheometrics fluid spectrometer). The shear rate ($\dot{\gamma}$) dependence of the steady-state viscosity (η) was measured for different volume fractions (fig. S5). This variation can be explained with the help of Cross model

$$\eta = \eta_\infty + \frac{\eta_0 - \eta_\infty}{1 + (C\dot{\gamma})^m} \tag{11}$$

where η_0 and η_∞ are the zero and infinity shear viscosity, respectively. The parameter m and C are known as the cross rate constant and cross time constant, respectively. By analyzing the experimental data with cross model, one can get the value of zero shear viscosity, which is shown as a function of volume fraction ϕ in Fig. 4B.

SUPPLEMENTARY MATERIALS
Supplementary material for this article is available at http://advances.sciencemag.org/cgi/content/full/6/3/eaaw9733/DC1

Fig. S1. Variation of $f(q, \tau)$ as a function of $\tau . q^2$ for different q's, which are collapsing together (ϕ = 0.0002 and azimuthal angle θ = −10°) as the diffusion coefficient is independent of q in $2\,\mu m^{-1} < q < 5\,\mu m^{-1}$ range.
Fig. S2. Variation of diffusion coefficients at ϕ = 0.0002.
Fig. S3. Variation of stretching exponent β as a function of ϕ from semi-dilute and concentrated regime.
Fig. S4. Variation of the structure factor at various ϕ (0.004 < ϕ < 0.3).
Fig. S5. Symbols represent the variation of viscosity as a function of shear rates for different volume fractions, whereas the continuous lines show the fits of the experimental data with the Cross model.

REFERENCES AND NOTES
1. M. P. Lettinga, E. Barry, Z. Dogic, Self-diffusion of rod-like viruses in the nematic phase. *Europhys. Lett.* **71**, 692–698 (2005).
2. M. P. B. van Bruggen, H. N. W. Lekkerkerker, G. Maret, J. K. G. Dhont, Long-time translational self-diffusion in isotropic and nematic dispersions of colloidal rods. *Phys. Rev. E* **58**, 7668–7677 (1998).
3. E. Pouget, E. Grelet, M. sP. Lettinga, Dynamics in the smectic phase of stiff viral rods. *Phys. Rev. E* **84**, 041704 (2011).
4. L. Alvarez, M. P. Lettinga, E. Grelet, Fast diffusion of long guest rods in a lamellar phase of short host particles. *Phys. Rev. Lett.* **118**, 178002 (2017).
5. M. P. B. van Bruggen, H. N. W. Lekkerkerker, J. K. G. Dhont, Long-time translational self-diffusion in isotropic dispersions of colloidal rods. *Phys. Rev. E* **56**, 4394–4403 (1997).
6. C. K. Mishra, A. Rangarajan, R. Ganapathy, Two-step glass transition induced by attractive interactions in quasi-two-dimensional suspensions of ellipsoidal particles. *Phys. Rev. Lett.* **110**, 188301 (2013).
7. Z. Zheng, R. Ni, F. Wang, M. Dijkstra, Y. Wang, Y. Han, Structural signatures of dynamic heterogeneities in monolayers of colloidal ellipsoids. *Nat. Commun.* **5**, 3829 (2014).
8. Z. Zheng, Y. Han, Self-diffusion in two-dimensional hard ellipsoid suspensions. *J. Chem. Phys.* **133**, 124509 (2010).
9. Z. Zheng, F. Wang, Y. Han, Glass transitions in quasi-two-dimensional suspensions of colloidal ellipsoids. *Phys. Rev. Lett.* **107**, 065702 (2011).
10. D. Lehner, H. Lindner, O. Glatter, Determination of the translational and rotational diffusion coefficients of rodlike particles using depolarized dynamic light scattering. *Langmuir* **16**, 1689–1695 (2000).
11. J. Rodríguez-Fernández, J. Pérez-Juste, L. M. Liz-Marzán, P. R. Lang, Dynamic light scattering of short Au rods with low aspect ratios. *J. Phys. Chem. C* **111**, 5020–5025 (2007).
12. I. Martchenko, H. Dietsch, C. Moitzi, P. Schurtenberger, Hydrodynamic properties of magnetic nanoparticles with tunable shape anisotropy: Prediction and experimental verification. *J. Phys. Chem. B* **115**, 14838–14845 (2011).
13. A. M. Shetty, G. M. Wilkins, J. Nanda, M. J. Solomon, Multiangle depolarized dynamic light scattering of short functionalized single-walled carbon nanotubes. *J. Phys. Chem. C* **113**, 7129–7133 (2009).
14. D. Kleshchanok, M. Heinen, G. Nägele, P. Holmqvist, Dynamics of charged gibbsite platelets in the isotropic phase. *Soft Matter* **8**, 1584–1592 (2012).
15. A. Wierenga, A. P. Philipse, H. N. W. Lekkerkerker, D. V. Boger, Aqueous dispersions of colloidal boehmite: Structure, dynamics, and yield stress of rod gels. *Langmuir* **14**, 55–65 (1998).
16. R. Schilling, T. Scheidsteger, Mode coupling approach to the ideal glass transition of molecular liquids: Linear molecules. *Phys. Rev. E* **56**, 2932 (1997).
17. M. Letz, R. Schilling, A. Latz, Ideal glass transitions for hard ellipsoids. *Phys. Rev. E* **62**, 5173 (2000).
18. K. Kang, J. K. G. Dhont, Glass transition in suspensions of charged rods: Structural arrest and texture dynamics. *Phys. Rev. Lett.* **110**, 015901 (2013).
19. K. Kang, Glass transition of repulsive charged rods (fd-viruses). *Soft Matter* **10**, 3311–3324 (2014).
20. P. Pfleiderer, K. Milinkovic, T. Schilling, Glassy dynamics in monodisperse hard ellipsoids. *Europhys. Lett.* **84**, 16003 (2008).
21. R. Cerbino, V. Trappe, Differential dynamic microscopy: Probing wave vector dependent dynamics with a microscope. *Phys. Rev. Lett.* **100**, 188102 (2008).

22. M. Reufer, V. A. Martinez, P. Schurtenberger, W. C. Poon, Differential dynamic microscopy for anisotropic colloidal dynamics. *Langmuir* **28**, 4618–4624 (2012).

23. P. N. Segrè, S. P. Meeker, P. N. Pusey, W. C. Poon, Viscosity and structural relaxation in suspensions of hard-sphere colloids. *Phys. Rev. Lett.* **75**, 958–961 (1995).

24. A. J. Banchio, G. Nägele, J. Bergenholtz, Viscoelasticity and generalized Stokes–Einstein relations of colloidal dispersions. *J. Chem. Phys.* **111**, 8721–8740 (1999).

25. A. J. Banchio, G. Nägele, Short-time transport properties in dense suspensions: From neutral to charge-stabilized colloidal spheres. *J. Chem. Phys.* **128**, 104903 (2008).

26. B. J. Berne, R. Pecora, *Dynamic Light Scattering: With Applications to Chemistry, Biology, and Physics* (Courier Corporation, 2000).

27. M. Reufer, H. Dietsch, U. Gasser, B. Grobety, A. M. Hirt, V. K. Malik, P. Schurtenberger, Magnetic properties of silica coated spindle-type hematite particles. *J. Phys. Condens. Matter* **23**, 065102 (2011).

28. M. Reufer, H. Dietsch, U. Gasser, A. Hirt, A. Menzel, P. Schurtenberger, Morphology and orientational behavior of silica-coated spindle-type hematite particles in a magnetic field probed by small-angle x-ray scattering. *J. Phys. Chem. B* **114**, 4763–4769 (2010).

29. I. Martchenko, J. J. Crassous, A. M. Mihut, E. Bialik, A. M. Hirt, C. Rufier, A. Menzel, H. Dietsch, P. Linse, P. Schurtenberger, Anisotropic magnetic particles in a magnetic field. *Soft Matter* **12**, 8755–8767 (2016).

30. P. Ilg, Anisotropic diffusion in nematic liquid crystals and in ferrofluids. *Phys. Rev. E* **71**, 051407 (2005).

31. F. Giavazzi, D. Brogioli, V. Trappe, T. Bellini, R. Cerbino, Scattering information obtained by optical microscopy: Differential dynamic microscopy and beyond. *Phys. Rev. E* **80**, 031403 (2009).

32. L. G. Wilson, V. A. Martinez, J. Schwarz-Linek, J. Tailleur, G. Bryant, P. Pusey, W. C. Poon, Differential dynamic microscopy of bacterial motility. *Phys. Rev. Lett.* **106**, 018101 (2011).

33. V. A. Martinez, R. Besseling, O. A. Croze, J. Tailleur, M. Reufer, J. Schwarz-Linek, L. G. Wilson, M. A. Bees, W. C. Poon, Differential dynamic microscopy: A high-throughput method for characterizing the motility of microorganisms. *Biophys. J.* **103**, 1637–1647 (2012).

34. G. Nägele, On the dynamics and structure of charge-stabilized suspensions. *Phys. Rep.* **272**, 215–372 (1996).

35. P. N. Segrè, P. N. Pusey, Scaling of the dynamic scattering function of concentrated colloidal suspensions. *Phys. Rev. Lett.* **77**, 771–774 (1996).

36. W. van Megen, R. H. Ottewill, S. M. Owens, P. N. Pusey, Measurement of the wave-vector dependent diffusion coefficient in concentrated particle dispersions. *J. Chem. Phys.* **82**, 508–515 (1985).

37. B. M. Fine, A. Lomakin, O. O. Ogun, G. B. Benedek, Static structure factor and collective diffusion of globular proteins in concentrated aqueous solution. *J. Chem. Phys.* **104**, 326–335 (1996).

38. M. Adam, M. Delsanti, Dynamical properties of polymer solutions in good solvent by rayleigh scattering experiments. *Macromolecules* **10**, 1229–1237 (1977).

39. U. Zettl, S. T. Hoffmann, F. Koberling, G. Krausch, J. Enderlein, L. Harnau, M. Ballauff, Self-diffusion and cooperative diffusion in semidilute polymer solutions as measured by fluorescence correlation spectroscopy. *Macromolecules* **42**, 9537–9547 (2009).

40. H. Vogel, The temperature dependence law of the viscosity of liquids. *Phys. Z.* **22**, 645 (1921).

41. G. S. Fulcher, Analysis of recent measurements of the viscosity of glasses. *J. Am. Ceram. Soc.* **8**, 339–355 (1925).

42. G. Tammann, W. Hesse, The dependence of viscosity upon the temperature of supercooled liquids. *Z. Anorg. Allg. Chem.* **156**, 245–257 (1926).

43. G. Brambilla, D. El Masri, M. Pierno, L. Berthier, L. Cipelletti, G. Petekidis, A. B. Schofield, Probing the equilibrium dynamics of colloidal hard spheres above the mode-coupling glass transition. *Phys. Rev. Lett.* **102**, 085703 (2009).

44. J. Mattsson, H. M. Wyss, A. Fernandez-Nieves, K. Miyazaki, Z. Hu, D. R. Reichman, D. A. Weitz, Soft colloids make strong glasses. *Nature* **462**, 83–86 (2009).

45. M. J. Solomon, D. V. Boger, The rheology of aqueous dispersions of spindle-type colloidal hematite rods. *J. Rheol.* **42**, 929–949 (1998).

46. C. De Michele, R. Schilling, F. Sciortino, Dynamics of uniaxial hard ellipsoids. *Phys. Rev. Lett.* **98**, 265702 (2007).

47. A. Pal, T. Zinn, M. Arif Kamal, T. Narayanan, P. Schurtenberger, Anomalous dynamics of magnetic anisotropic colloids studied by xpcs. *Small* **14**, e1802233 (2018).

48. M. Ocaña, M. P. Morales, C. J. Serna, Homogeneous precipitation of uniform α-Fe$_2$O$_3$ particles from iron salts solutions in the presence of urea. *J. Colloid Interface Sci.* **212**, 317–323 (1999).

49. C. Graf, D. L. J. Vossen, A. Imhof, A. van Blaaderen, A general method to coat colloidal particles with silica. *Langmuir* **19**, 6693–6700 (2003).

50. S. R. Parnell, A. L. Washington, A. J. Parnell, A. Walsh, R. M. Dalgliesh, F. Li, W. A. Hamilton, S. Prevost, J. P. A. Fairclough, R. Pynn, Porosity of silica Stöber particles determined by spin-echo small angle neutron scattering. *Soft Matter* **12**, 4709–4714 (2016).

ScienceAdvances

Anisotropic dynamics and kinetic arrest of dense colloidal ellipsoids in the presence of an external field studied by differential dynamic microscopy

Antara Pal, Vincent A. Martinez, Thiago H. Ito, Jochen Arlt, Jérôme J. Crassous, Wilson C. K. Poon and Peter Schurtenberger

ARTICLE TOOLS	http://advances.sciencemag.org/content/6/3/eaaw9733
SUPPLEMENTARY MATERIALS	http://advances.sciencemag.org/content/suppl/2020/01/13/6.3.eaaw9733.DC1
REFERENCES	This article cites 48 articles, 0 of which you can access for free http://advances.sciencemag.org/content/6/3/eaaw9733#BIBL
PERMISSIONS	http://www.sciencemag.org/help/reprints-and-permissions

Use of this article is subject to the Terms of Service